NAVAL POSTGRADUATE SCHOOL

MONTEREY, CALIFORNIA

THESIS

DEVELOPMENT OF A NUMERICAL TOW TANK WITH WAVE GENERATION TO SUPPLEMENT EXPERIMENTAL EFFORTS

by

Leo M. Jones

December 2017

Thesis Co-Advisors: Young Kwon
Joseph Klamo

THIS PAGE INTENTIONALLY LEFT BLANK

REPORT DOCUMENTATION PAGE

Form Approved OMB No. 0704–0188

1. AGENCY USE ONLY *(Leave Blank)*	2. REPORT DATE	3. REPORT TYPE AND DATES COVERED
	December 2016	Master's Thesis 07-05-2016 to 12-09-2017

4. TITLE AND SUBTITLE

DEVELOPMENT OF A NUMERICAL TOW TANK WITH WAVE GENERATION TO SUPPLEMENT EXPERIMENTAL EFFORTS

5. FUNDING NUMBERS

6. AUTHOR(S)

Leo M. Jones

7. PERFORMING ORGANIZATION NAME(S) AND ADDRESS(ES)

Naval Postgraduate School
Monterey, CA 93943

8. PERFORMING ORGANIZATION REPORT NUMBER

9. SPONSORING / MONITORING AGENCY NAME(S) AND ADDRESS(ES)

N/A

10. SPONSORING / MONITORING AGENCY REPORT NUMBER

11. SUPPLEMENTARY NOTES

The views expressed in this document are those of the author and do not reflect the official policy or position of the Department of Defense or the U.S. Government. IRB Protocol Number: N/A.

12a. DISTRIBUTION / AVAILABILITY STATEMENT

Approved for public release. Distribution is unlimited.

12b. DISTRIBUTION CODE

13. ABSTRACT *(maximum 200 words)*

This research investigates the capability of computational fluid dynamics to accurately model the performance of a vertically oscillating wave-generating wedge and resultant wave-induced loads on a submerged object in a tow tank. Specifically, the wave height, wave frequency, and unsteady forces on a submerged body were determined from numerous simulations and compared to experimentally measured data from nearly identical conditions as the simulations. Time histories of the water surface elevation were experimentally measured at various fixed locations in the tank to characterize the wave propagation. Once the wave environment was verified as being accurately captured, a fully submerged body was included in the experimental and simulated tanks. Identical waves were generated in both the physical and numerical environments, and passed over a square cross section submerged body that was located near-surface. The experimentally measured and numerically simulated unsteady forces and moments on the body were compared. The model captured loads experienced by the body quite accurately at low wavelengths, yet overestimated loads at higher wavelengths. Future studies should further refine simulation mesh resolution and investigate loads experienced by different geometries at a variety of depths to better understand over-prediction at large wavelengths.

14. SUBJECT TERMS

numerical wave generation, wedge-shaped wave maker, computational fluid dynamics, CFD, loads on near-surface submerged body

15. NUMBER OF PAGES 67

16. PRICE CODE

17. SECURITY CLASSIFICATION OF REPORT	18. SECURITY CLASSIFICATION OF THIS PAGE	19. SECURITY CLASSIFICATION OF ABSTRACT	20. LIMITATION OF ABSTRACT
Unclassified	Unclassified	Unclassified	UU

NSN 7540-01-280-5500

Standard Form 298 (Rev. 2–89)
Prescribed by ANSI Std. 239–18

THIS PAGE INTENTIONALLY LEFT BLANK

Approved for public release. Distribution is unlimited.

DEVELOPMENT OF A NUMERICAL TOW TANK WITH WAVE GENERATION TO SUPPLEMENT EXPERIMENTAL EFFORTS

Leo M. Jones
Ensign, United States Navy
B.S., United States Naval Academy, 2016

Submitted in partial fulfillment of the
requirements for the degree of

MASTER OF SCIENCE IN MECHANICAL ENGINEERING

from the

NAVAL POSTGRADUATE SCHOOL
December 2017

Approved by: Young Kwon
Thesis Co-Advisor

Joseph Klamo
Thesis Co-Advisor

Garth Hobson
Chair, Department of Mechanical and Aerospace Engineering

THIS PAGE INTENTIONALLY LEFT BLANK

ABSTRACT

This research investigates the capability of computational fluid dynamics to accurately model the performance of a vertically oscillating wave-generating wedge and resultant wave-induced loads on a submerged object in a tow tank. Specifically, the wave height, wave frequency, and unsteady forces on a submerged body were determined from numerous simulations and compared to experimentally measured data from nearly identical conditions as the simulations. Time histories of the water surface elevation were experimentally measured at various fixed locations in the tank to characterize the wave propagation. Once the wave environment was verified as being accurately captured, a fully submerged body was included in the experimental and simulated tanks. Identical waves were generated in both the physical and numerical environments, and passed over a square cross section submerged body that was located near-surface. The experimentally measured and numerically simulated unsteady forces and moments on the body were compared. The model captured loads experienced by the body quite accurately at low wavelengths, yet overestimated loads at higher wavelengths. Future studies should further refine simulation mesh resolution and investigate loads experienced by different geometries at a variety of depths to better understand over-prediction at large wavelengths.

THIS PAGE INTENTIONALLY LEFT BLANK

Table of Contents

List of Figures

List of Tables

THIS PAGE INTENTIONALLY LEFT BLANK

List of Acronyms and Abbreviations

ASW	anti-submarine warfare
ASuW	anti-surface warfare
AUVs	autonomous undersea vehicles
CAD	computer aided design
CFD	computational fluid dynamics
FVM	finite volume method
IO	information operations
ISR	intelligence, surveillance, and reconnaissance
MCM	mine countermeasures
NPS	Naval Postgraduate School
RANS	Reynolds-averaged Navier-Stokes
SPH	smoothed particle hydrodynamics
TCS	time critical strike
UUVs	unmanned undersea vehicles

THIS PAGE INTENTIONALLY LEFT BLANK

Acknowledgments

I would like to thank both of my advisors, Dr. Kwon and Dr. Klamo. Without their guidance, I would have accomplished far less with far more effort. Their steadfast support pushed me to deliver a product that I am truly proud of.

THIS PAGE INTENTIONALLY LEFT BLANK

CHAPTER 1:
Introduction

1.1 Importance of Tow Tank Testing

Modern naval architecture and marine engineering necessitates the use of parametric experimentation to develop hydrodynamically effective vessels and structures. Historically, these experiments have been done in tow tanks. In such an experimental domain, conditions such as the wave environment, vessel orientation, and testing speeds are easily controlled to produce indispensable data. Tow tank data has evolved to include ship performance in waves, wake studies, and stability of submerged vessels. The future of developments in naval architecture will require the tow tank to be an invaluable piece of equipment for testing the seaworthiness of vessel hull shapes prior to their full-scale development.

1.2 NPS Tow Tank

The Naval Postgraduate School (NPS) has a small tow tank built in the 1970s. This 10.97 meter (36 foot) long facility is short by academic standards and has lacked wave generation capabilities since its conception. Experiments were limited to towing small-scale models of ship hulls at low speeds in calm water. Displayed in Figure 1.1, the Halligan Hall tow tank features a carriage tow plate mounted on rails in the middle of the tank.

Figure 1.1. NPS Halligan Hall tow tank before wedge installation.

In 2016, NPS student Ensign Ryan Tran adapted an existing vertical plunging wedge wave maker design used at the U.S. Naval Academy to the NPS tow tank, thus adding wave testing to the tank's experimental capabilities [1]. The fully installed wedge is shown in Figure 1.2. However, the tank still lacked the instrumentation to record wave behavior, specifically wave height over time. Additionally, the tank was without equipment that would record multi-axial transient hull forces resulting from the waves.

Efforts have been made to expand the capabilities of the testing facility, but these additions are time consuming, and in many cases, expensive. The ability to monitor phenomena such as wakes, turbulence, multi-axis loads, and vessel orientation require a considerable amount of engineering creativity. In many cases, observation of these parameters interferes with the testing environment. Limitations in the physical testing environment necessitate the use of numerical studies to augment experimental results.

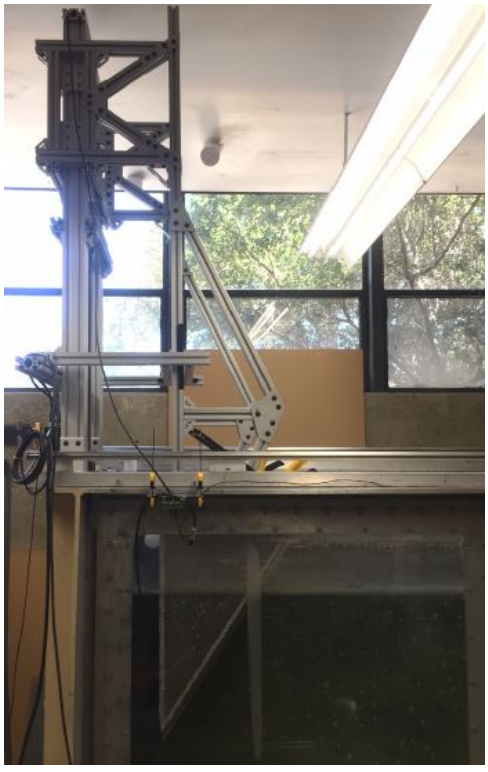

Figure 1.2. Side view of wedge wave maker system.

1.3 Numerical Study

Numerical methods of studying fluid dynamics are a relatively new approach of modeling fluid behavior in a virtual domain. Computational fluid dynamics (CFD) has provided engineers with the ability to conduct preliminary studies of fluid environments without running physical experiments. Numerical models allow the comparison of geometries in their respective operating environments without intrusive measuring equipment. Computational fluid models allow investigation of fluid conditions in great detail by producing outputs such as velocity and pressure fields. Simulated geometries may include ship hulls, submarine hulls, lifting surfaces, or turbomachinery, among endless other examples. Modern computers are powerful enough and CFD has matured such that meaningful calculations can be made on a single desktop computer using one of dozens of CFD software packages.

An advantage of numerical study is that a user may manipulate the environment physics to suit the needs of the test. This capability may be extremely expensive or impossible in the physical domain. While a tow tank has a finite depth (which may impact results, however slightly), a numerical environment may run simulations in an environment of infinite depth and width. Additionally, parameters such as viscosity may be altered in order to study the magnitude of its effect on results.

The speed at which geometries may be created and analyzed in a CFD environment is generally much faster than those geometries may be physically produced and observed. Even with modern fabrication methods such as 3D printing, scale-models can take days to weeks to produce, even with the requisite CAD files on hand. In a computational domain, geometries can be rapidly created or altered in a CAD software, then simply uploaded to a CFD program for analysis.

1.4 Motivation

Current efforts involve developing an accurate replication of the NPS tow tank and oscillating wedge in a virtual environment. The numerical domain must first be verified as an accurate representation of the physical world, specifically in respect to the studies that the tank is currently being used to conduct.

1.4.1 Difficulties Encountered with Unsteady Vertical Loads

In an increasingly clandestine world, an unsurpassed number of naval operations are being done beneath the surface of the sea. Submarines have proven themselves important and capable as ever in the realms of anti-submarine warfare (ASW), anti-surface warfare (ASuW), and strategic deterrence. The U.S. Navy is investing billions of dollars into a future that involves heavy use of unmanned undersea vehicles (UUVs) and autonomous undersea vehicles (AUVs). These vehicles, which will range from the size of a football to the size of a school bus, have already found their niche in oceanography, bathymetry, communication, payload delivery, mine countermeasures (MCM), intelligence, surveillance, and reconnaissance (ISR), information operations (IO), time critical strike (TCS), and ASW [2]. Many undersea operations for UUVs and submarines must be done near the surface, oftentimes in heavy seas and at a forward velocity. In such cases, the effects that the sea state has on the depth control of the vehicle cannot be ignored. Mission success may depend upon the ability of the vehicle to not only stay completely submerged, but also maintain depth within a small margin.

Unfortunately, waves make this task difficult, especially for smaller vehicles. Orbital velocities of water particles become increasingly significant close to the surface. This increased orbital velocity translates to unsteady forces on a near-surface vehicle, which has the potential to cause a surface breach.

1.4.2 Long-Term Goal

The ocean environment is complex, made up of many waveforms. Traditionally, it is decomposed into a superposition of individual waveforms. If the loads caused by a single waveform can be understood and predicted, they could then be combined in the appropriate manner to predict loads in a realistically complex environment. If this process could be done in real-time, predictive control algorithms could be developed. Near-surface vehicles utilizing such an algorithm would be able to adjust their control surfaces in anticipation of transient loads resulting from passing surface waves, effectively mitigating the surfacing effects.

Wave tanks such as the one at NPS will prove vital in developing such algorithms. Once the numerical testing environment is validated for waves passing over a square cross sectional

body, simulations can be expanded to include testing of curved or axisymmetric bodies in simple and complex waveforms. An understanding of the contribution of each individual waveform is then necessary to accurately predict loads on a vehicle. Once the relationship between constituent waves and transient loads on a particular vehicle geometry is thoroughly understood, predictive algorithms may be developed to counter these loads.

1.5 Objective

The objective of this study is to assess the accuracy of the numerical wedge-driven wave tank in terms of wave structure and resultant forces on submerged bodies, specifically in the environment of the NPS tow tank. To accomplish this objective, a numerical wave tank was created and validated with experimental results. The accuracy of simulated loads on a near-surface body in the validated wave tank was then assessed.

1.5.1 Experimental Approach

Experimental data to include wave elevation and multi-axis loads on a submerged body was necessary to validate the numerical tank. The NPS tow tank has recently been modernized accordingly. As previously stated, an oscillating wedge accompanies a motor, controller, and actuator as the wave-generating mechanism. Ultrasonic probes have been placed at various locations along the tank to record wave height at discrete time intervals. Load cells attached to a submerged axisymmetric body measure transient loads experienced by the body.

1.5.2 Numerical Approach

The physical tow tank has been rendered as a CAD model with the exact dimensions of the tank and wedge. Wedge motion functions identical to those used in the physical domain were observed, and the resulting wave heights and frequencies were compared to those generated experimentally. A temporal and spatial resolution study was then conducted to determine the optimal simulation parameters for this particular study. Heights of waves generated by various wedge inputs were observed and a transfer function relating wave height to wedge amplitude was developed. A square cross section geometry was then rendered and inserted into the fluid domain. Waves of varying shape were generated and resultant transient loads

were observed. Geometries, transverse location of the submerged body, and depth of the submerged body were kept identical to parameters in the experimental domain.

CHAPTER 2:
Background and Literature Review

2.1 Linear Wave Theory and Dispersion Waves

Gravity-driven water waves can encompass a wide range of wavelengths. These different wavelengths propagate at different speeds, and similar wavelengths will interfere with each other. The resultant wave structure has a distinct phase speed and group speed. The phase speed is the speed of the individual ripples in a wave set. These are easy to visually observe in an environment such as a wave tank. The group speed is the speed of the envelope or the speed of disturbance. Figure 2.1 demonstrates the effect of different phase speeds causing spreading of the wave packet.

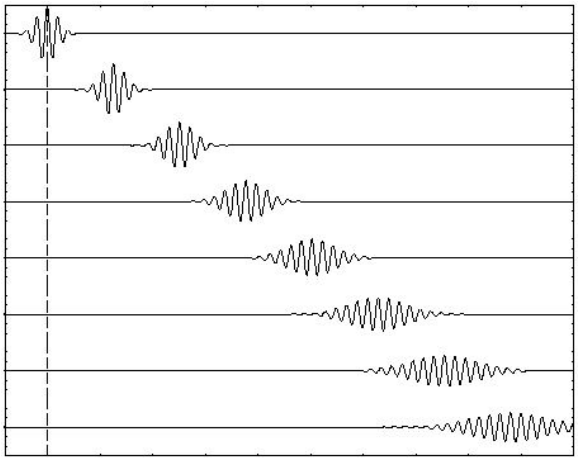

Figure 2.1. Difference in group and phase speed of dispersive wave packet. Source: [3].

The equations relating wavelength, wave period, phase speed, and group speed are different depending upon water depth. In shallow water (depth less than 5% the wavelength), the waves interact with the bottom, influencing wave behavior. Once the water exceeds a certain depth (about half of the wavelength of the surface waves) the bottom interaction is negligible. Waves in water between 5% and 50% of the wavelength are considered intermediate waves

and follow a third set of relations. The dispersion relations are shown in Table 2.1. These relations are derived from linear wave theory in an inviscid fluid.

parameter	symbol
angular frequency	ω
frequency	f
group velocity	c_g
period	T
phase velocity	c_p
water depth	d
wavelength	λ
wave number	k

$$k = \frac{2\pi}{\lambda}$$
$$\omega = 2\pi f$$
$$f = \frac{1}{T}$$

quantity	deep water $d > 0.5\lambda$	intermediate $0.05\lambda > d > 0.5\lambda$	shallow $0.05\lambda > d$
λ	$\frac{g}{2\pi}T^2$	$\left(\frac{2\pi}{T}\right)^2 = \frac{2\pi g}{\lambda}\tanh\left(\frac{2\pi d}{\lambda}\right)$	$T\sqrt{gd}$
c_p	$\frac{g}{2\pi}T$	$\sqrt{\frac{g}{k}\tanh(kd)}$	$\sqrt{gd}$
c_g	$\frac{g}{4\pi}T$	$\frac{1}{2}c_p\left(1 + \frac{2kd}{\sinh(2kd)}\right)$	$\sqrt{gd}$

Table 2.1. Surface wave dispersion equations.

2.1.1 Steepness Limitations

Wave amplitude and wavelength are individual parameters and can be specified independently of each other up to a certain limit. For a given wavelength, the amplitude can take on any value up to the limit that causes the crest of a wave of that wavelength to break. That limit is known as the wave steepness, H/λ. If a wave becomes too steep, it will break. The theoretical maximum steepness of periodic deep water waves according to Stokes Wave Theory is 1/7 [4]. In reality, the theoretical wave steepness can never be reached, and a practical wave steepness of 1/10 is commonly used. Decreased critical wave steepness is due to imperfections and noise in the experimental facility.

2.1.2 Stokes Waves

Rather than behaving like simple, sinusoidal waves, waves of steepness greater than 1/20 behave according to Stokes Wave Theory [5]. Stokes waves are asymmetric about the calm water surface in that the crests are high and narrow while the troughs are shallow and wide. This asymmetry is due to the constant downward force of gravity on the fluid. Since the wave conditions investigated in this study were fairly steep, an asymmetric wave profile was observed. This behavior was captured using a third-order Stokes wave approximation. Accordingly, the Stokes wave height is approximated as

$$H = 2a\left(1 + \frac{3}{8}k^2a^2\right) \tag{2.1}$$

where a is the first order sine wave amplitude and k is the wave number.

2.2 Prior Work in Numerical Wave Tanks and Near-Surface Loads

Studies have previously been done to examine the efficacy of capable numerical models of wave tanks. Additionally, a great deal of effort has gone into investigating the theory behind vertical forces acting on near-surface bodies.

2.2.1 Numerical Wave Generation

Finnegan and Goggins conducted numerical wave tank simulations of a flapper type wave maker in a tank with a sloped beach using ANSYS CFX [6]. Specifically, they investigated two-dimensional models and compared the results of the wave structure to those generated by wave maker theory, and the water particle velocities were compared to linear wave theory. No experimentally generated results were used for comparison in this study.

Yim et al. conducted a study comparing two numerical methods to waves experimentally generated by a free falling rigid body [7]. The study determined that the two models, Reynolds-averaged Navier-Stokes (RANS) and smoothed particle hydrodynamics (SPH), sufficiently modeled "the free surface elevation time series" in a two-dimensional environment where the wave generation mechanism is a free falling cylinder.

Galdelho et al. investigated the accuracy of numerically generated waves in a wedge type wave tank where an absorbing beach was present [8]. The CFD software used in this study was OpenFOAM. Vertical wedge force and wave heights were recorded. Numerical data was then compared to corresponding experimental data. Various wedge frequencies and amplitudes were used. Results of this study revealed that the particular setup of the CFD software produced numerical waves that were slightly smaller in height than the physical waves, but overall very similar in structure.

2.2.2 Loads on Near-Surface Submerged Bodies

Numerous experimental studies have been conducted to examine the effects of waves on submerged bodies of various geometries. Alvarez, Bertram, and Gualdesi compare axisymmetric hull shapes of a submerged body with respect to minimizing skin friction, form resistance, and wave resistance [9]. Simple time stepping of a modified simulated annealing technique was validated with experimental results to determine the more efficient hull shape. The study was carried out in calm water and vertical forces on the hulls were not considered.

The David Taylor Model Basin (currently Naval Surface Warfare Center Carderock Division) conducted a study in 1954 that derived the theoretical first-order forces and moments on a body of revolution under a sinusoidal wave in an inviscid fluid and compared this to experimentally measured loads [10]. Forces and moments acting on a model of a GUPPY

submarine hull were observed and found to be in alignment with the classical lift equations for the hull geometry and wave characteristics, despite substantial experimental scatter.

Khalil conducted an experimental study in which waves were passed transversely over a submerged cylinder at varying depths [11]. A load cell measured mean vertical and horizontal forces over the cylinder. Transient forces were found to follow a near-first-order profile, unless waves were breaking, thus introducing nonlinear wave forces. These nonlinear effects were amplified as the cylinder was brought closer to the surface. This study did not produce a well-defined relationship between wave behavior, depth, and geometry to observed body force.

Previous studies investigating the forces observed by bodies in a three-dimensional CFD simulation of a wedge type wave tank are limited. Most existing evaluations of numerical wave tanks are done in two dimensions. ANSYS CFX must be validated specifically in the three-dimensional environment before more complicated tests may be carried out. The current study addresses these limitations.

2.3 Numerical Methods

The basis of computational fluid dynamics involves first rendering a fluid domain in a computer aided design (CAD) program, then discretizing that domain into a user-defined number of small elements. Boundary conditions of the fluid domain are then defined and the Navier-Stokes equations are evaluated iteratively in each element. Simulations can be run for both steady state and transient problems, whereby the Navier-Stokes equations are applied for each user-defined time step.

2.3.1 Navier-Stokes Equations

The three-dimensional unsteady Navier-Stokes equations are presented in Equation (2.2) through Equation (2.6). Equation (2.2) is the continuity equation. Equation (2.3) to Equation (2.5) are the momentum equations in the x, y, and z directions, respectively. Equation (2.6) is the energy equation. All equations are in their conservation form [12].

$$\frac{\partial \rho}{\partial t} + \frac{\partial (\rho u)}{\partial x} + \frac{\partial (\rho v)}{\partial y} + \frac{\partial (\rho w)}{\partial z} = 0 \tag{2.2}$$

$$\frac{\partial(\rho u)}{\partial t} + \frac{\partial(\rho u^2)}{\partial x} + \frac{\partial(\rho uv)}{\partial y} + \frac{\partial(\rho uw)}{\partial z} = X - \frac{\partial p}{\partial x} + \frac{1}{Re}\left(\frac{\partial \tau_{xx}}{\partial x} + \frac{\partial \tau_{xy}}{\partial y} + \frac{\partial \tau_{xz}}{\partial z}\right) \tag{2.3}$$

$$\frac{\partial(\rho v)}{\partial t} + \frac{\partial(\rho uv)}{\partial x} + \frac{\partial(\rho v^2)}{\partial y} + \frac{\partial(\rho vw)}{\partial z} = Y - \frac{\partial p}{\partial y} + \frac{1}{Re}\left(\frac{\partial \tau_{xy}}{\partial x} + \frac{\partial \tau_{yy}}{\partial y} + \frac{\partial \tau_{yz}}{\partial z}\right) \tag{2.4}$$

$$\frac{\partial(\rho w)}{\partial t} + \frac{\partial(\rho uw)}{\partial x} + \frac{\partial(\rho vw)}{\partial y} + \frac{\partial(\rho w^2)}{\partial z} = Z - \frac{\partial p}{\partial z} + \frac{1}{Re}\left(\frac{\partial \tau_{xz}}{\partial x} + \frac{\partial \tau_{yz}}{\partial y} + \frac{\partial \tau_{zz}}{\partial z}\right) \tag{2.5}$$

$$\begin{aligned}\frac{\partial(E_T)}{\partial t} + \frac{\partial(uE_T)}{\partial x} + \frac{\partial(vE_T)}{\partial y} + \frac{\partial(wE_T)}{\partial z} &= -\frac{\partial(up)}{\partial x} - \frac{\partial(vp)}{\partial y} - \frac{\partial(wp)}{\partial z} \\ &- \frac{1}{RePr}\left(\frac{\partial q_x}{\partial x} + \frac{\partial q_y}{\partial y} + \frac{\partial q_z}{\partial z}\right) + \frac{1}{Re}\left[\frac{\partial}{\partial x}(u\tau_{xx} + v\tau_{xy} + w\tau_{xz})\right. \\ &\left. + \frac{\partial}{\partial y}(u\tau_{xy} + v\tau_{yy} + w\tau_{yz}) + \frac{\partial}{\partial z}(u\tau_{xz} + v\tau_{yz} + w\tau_{zz})\right]\end{aligned} \tag{2.6}$$

where *(x,y,z)* are position components, *(u,v,w)* are velocity components, t is time, ρ is fluid density, p is pressure, τ is fluid shear stress, Re is Reynolds number, Pr is the Prandtl number, E_T is total energy, X, Y, and Z are fluid body forces, and q is heat flux [13].

2.3.2 Finite Volume Method

ANSYS CFX, the CFD software used in this study, uses a finite volume method (FVM) to achieve a numerical solution [12]. The FVM involves discretizing the fluid domain into small elements, or control volumes. Figure 2.2 shows such a two-dimensional element. The array of elements is referred to as the domain mesh. The governing differential equations (unsteady Navier-Stokes equations) are then integrated over each element to determine fluid state values at all discrete points in the mesh [12]. Mass, momentum, and energy are conserved inside each control volume. In transient simulations, a differential time stepping

scheme is used to evaluate fluid properties at each user-defined time step [14].

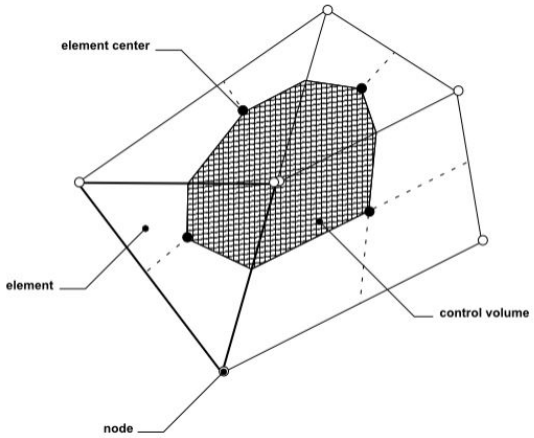

Figure 2.2. Illustration of a two-dimensional finite volume element used by ANSYS CFX to apply conservation laws and numerically solve for fluid properties. Source: [12].

FVM is the most commonly used numerical method for current CFD packages. It is able to achieve high accuracy solutions with comparatively low computational time. The FVM allows great flexibility when structuring the mesh and may be applied to both two-dimensional and three-dimensional simulations [14]. These advantages make this method ideal for the current study.

THIS PAGE INTENTIONALLY LEFT BLANK

CHAPTER 3:
Experimental Setup

3.1 Description of Experimental Facility

The experimental tow tank is 10.97 meters (36.0 feet) long, 0.911 meters (3.0 feet) wide, and 1.219 meters (4.0 feet) deep. The tank is aluminum walled with Plexiglas windows on one side to allow observation. The tank has a maximum fill capacity of 9166.8 liters (2421.6 gallons) and is supported by I-beams that span the length of the tank. For this study, the tank was filled with fresh water and was kept at a depth of 0.91 meters (3.0 feet). The wave maker system is mounted near the end of the tank.

3.2 Wave Maker Setup and Actuation

The tank's wave maker is the product of former NPS student Ensign Ryan Tran. The system is based on a similar wave maker used at the U.S. Naval Academy by the Naval Architecture and Ocean Engineering department [1]. The 5086 marine grade aluminum wedge is slightly less than 0.911 meters (3.0 feet) wide to allow for clearance with the sides of the tank. It has a declination angle of 35 degrees from the vertical and is 0.610 meters (2.0 feet) in height. The geometry of the wedge is shown in Figure 3.1 and a side view of the wedge is shown in Figure 1.2.

The wedge was fabricated by the NPS Mechanical and Aerospace Engineering Machine shop by welding together four individual faces. To prevent leaking, the interior seams were coated with a marine sealant. Frequent cleanings of the wedge face were required to prevent fouling and corrosion. Consequently, the outside of the wedge was coated with Flex-Seal liquid rubber.

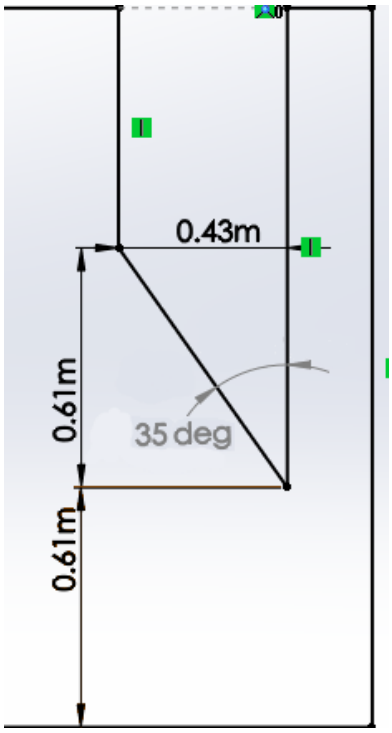

Figure 3.1. Dimensioned drawing of the wedge geometry used in experiments and numerical simulations.

The wedge creates waves by oscillating vertically. The wedge is attached to a support frame that is free to travel along two vertical rails using Teflon sliders. The frame is attached to a linear actuator and electric motor to provide oscillatory motion. Roller bearings prevent wedge motion in the transverse direction, keeping oscillations purely vertical. The frame was constructed of 80/20 prefabricated aluminum T-slot profiles and corresponding accessory pieces. The wedge support frame is shown in Figure 3.2.

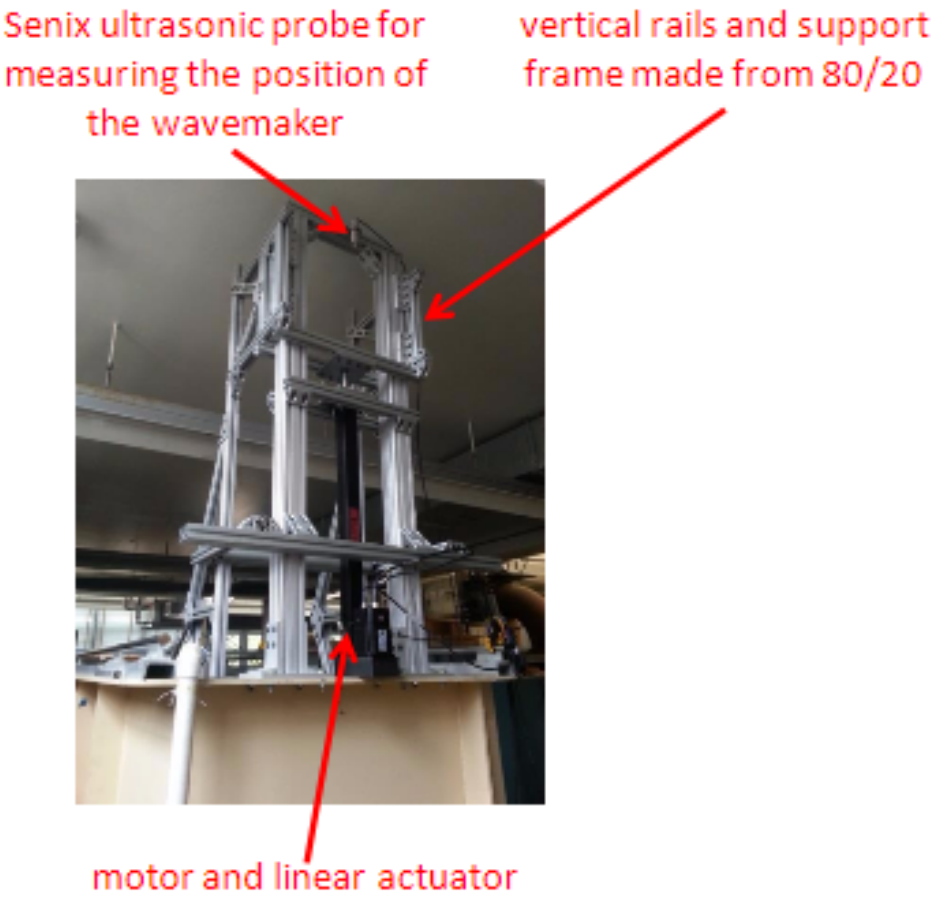

Figure 3.2. The frame supporting the wedge, made of 80/20 T-slotted aluminum profiles.

Motion of the wedge is controlled by a motor, controller, and linear actuator. The motor used is a MOOG - Animatics MT Motor, which provides a peak torque of 3.94 N-m (34.88 in-lb). It has a 1120 watts of peak power and a maximum rotational speed of 3330 rpm. The controller is a Modusystems Pulse/Dir controller MAC-2TC interfaced through Snap2Motion software. This software allows the user to easily and quickly define control parameters of wedge motion. The linear actuator is an E-Drive L-TAC LS long stroke ball screw linear actuator. It has a maximum stroke of 0.6096 meters (24 inches), a maximum thrust of 1779.3 newtons (400 pounds), and a maximum linear speed of 0.4064 m/s (16.0 in/s).

3.3 Data Collection

Senix ToughSonic ultrasonic probes are used to measure distance to a point of reflection. In this experiment, they were used to measure distance to the water surface and wedge motion. For the wedge, the Senix probe measured the distance to a piece of electrical tape placed along a horizontal arm of the support frame, while three additional probes were mounted at 2.74 meters (9.0 feet), 5.49 meters (18.0 feet), and 8.23 meters (27.0 feet) downstream from the wave maker. These distances correspond to nondimensionalized x/L values of 0.25, 0.50, and 0.75, where L is tank length.

An AMTI six-component MC3A load cell and Gen5 signal conditioner and amplifier measure all three components of force and moment observed by a submerged body. An aluminum sting is secured to the aft face of the body and the body center is set directly beneath the load cell. The signal conditioner collects the force and moment signals at a rate of 100 Hz so that they may be collected by a MATLAB collection routine. The load cell is shown attached to the tow tank carriage plate in Figure 3.3.

Commanded wedge displacement is sinusoidal. The user defines the amplitude, frequency, and phase of the commanded sine function in the Snap2Motion software. As the wedge oscillates, the MATLAB collection routine collects voltage readings from each probe at a user defined frequency (50 Hz for this study) for 60 seconds. Simultaneously, the force and moment readings from the load cell are collected and compiled. Probe, force, and moment voltages are compiled into a single comma-separated values file.

A post-collection analysis routine applies a gain to the probe voltage readings to produce wave elevation in inches, with the zero elevation point set prior to wave generation when the water is calm. A gain is applied to the load cell voltages to produce force and moment readings in units of pounds and inch-pounds, respectively. The gauge electrical offset is also removed using the results of the calm water zero file. The data is then compiled into a "cleaned" comma-separated values file with elevation, force, and moment in their appropriate units.

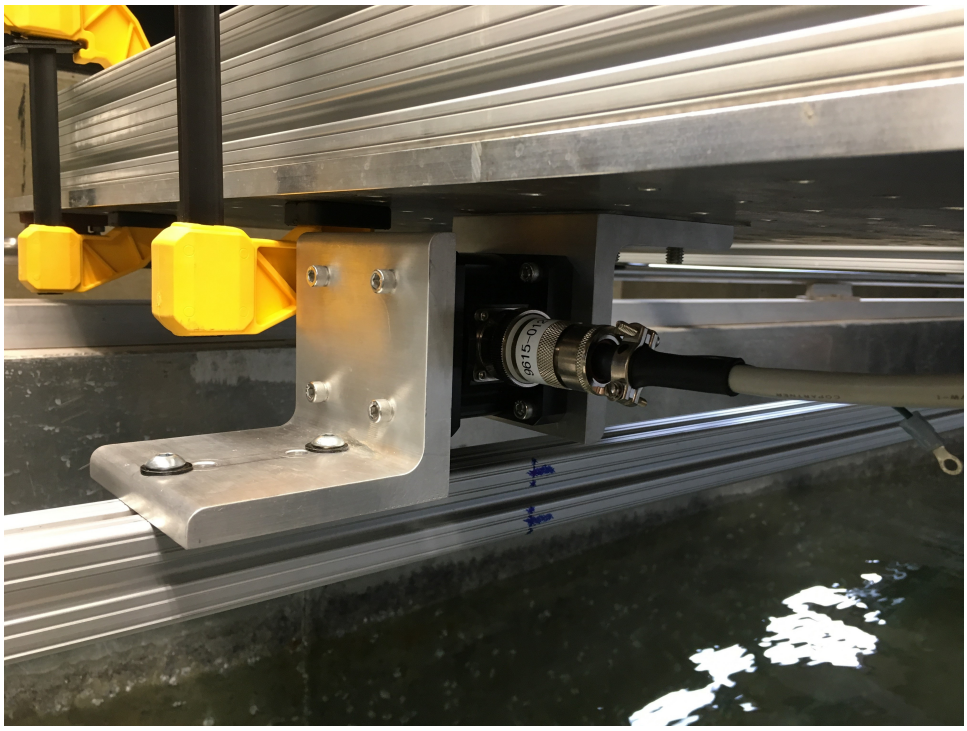

Figure 3.3. Load cell measures three-dimensional force and moments.

3.4 Wave Limitations

In order to not introduce the effects of shallow water into the investigation, efforts were made to ensure that waves analyzed were deep water waves. The rotating water particles of intermediate and shallow water waves interfere with the solid bottom, introducing extraneous nonlinear wave effects. Additionally, only non-breaking waves were analyzed to avoid interruptions of the periodicity of the waves.

3.4.1 Deep Water Limitations

Deep water waves are defined as waves that have wavelengths less than double the water depth [15]. The resting water depth of the NPS tow tank is 0.9144 meters (3.0 feet), meaning that maximum wavelength was 1.829 meters (6.0 feet). Applying the deep water dispersion relations outlined in Table 2.1, it is found that the minimum deep water wave frequency for the NPS tow tank is 0.924 Hz. Wave frequencies slightly below this limit were considered in

the study but the resultant calculated wavelength was corrected for non-deep water effects. The difference between the deep water wavelength and the corrected value for our lowest tested frequency was less than 1%.

3.4.2 Steepness Limitations

In order to keep the waves from breaking and disrupting the periodicity of generated waves, experimental inputs were kept such that steepness did not exceed the practical wave steepness limit of 1/10. Using this limit and a sine wave amplitude approximation, the relationship between wave amplitude and wavelength for non-breaking waves is defined in Equation (3.1).

$$\frac{2a}{\lambda} < \frac{1}{10} \tag{3.1}$$

3.4.3 Wedge Speed Limitations

The linear actuator that drives the wedge has a maximum operating speed of 40.64 cm/s (16.0 in/s). The wedge reaches its maximum speed as it is passing through the center of its stroke. In order to keep this speed below the maximum speed of the actuator, the amplitude and frequency must satisfy the following inequality.

$$a_w < \frac{0.406}{2\pi f} \tag{3.2}$$

where a_w is amplitude of the wedge oscillation in meters.

Figure 3.4 summarizes the amplitude and frequency operating limitations of the experimental wedge.

3.4.4 Run Time Limitations

The experimental study featured a simple beach at the end of the tank to dampen waves that reached the end wall. The numerical study, however, involved no beach to dampen waves once they reached the end of the tow tank. Waves completely reflected off of the end wall.

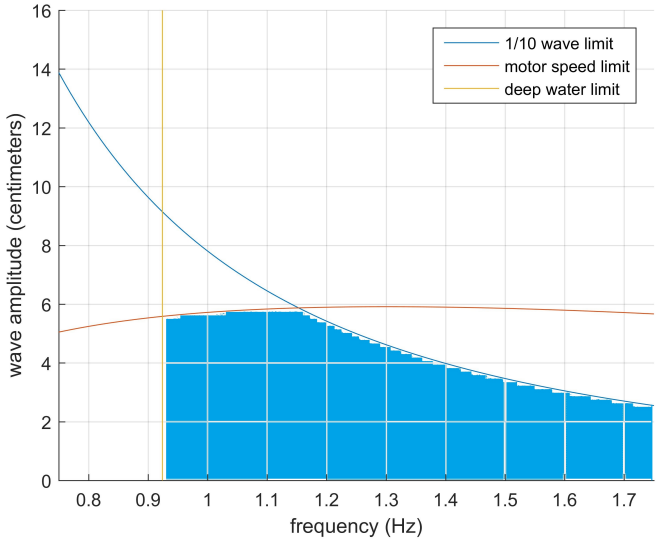

Figure 3.4. Inequality plot showing wedge operating conditions. Frequencies and amplitudes in the blue region may be used.

In order to remove wave reflection as a factor affecting wave behavior, simulations were ended before reflected waves reached the probes. Runs at the lowest allowable frequency, 0.924 Hz, propagate at a phase speed of 1.69 m/s. At this speed, the waves reach the end of the tank in 6.49 seconds. Higher frequencies would reach the end at an even later time. Simulations were run until reflected waves returned to the area of interest, or 16 seconds, whichever occurred first.

3.5 Testing Matrix

To determine the appropriate simulation parameters to apply, a parametric study comparing computationally generated waves to experimentally generated waves was done first. Factors such as mesh refinement, time step, and type of meshing method were varied while wedge motion was kept constant at 1 Hz frequency and 2.54 centimeters (1.0 inch) amplitude. Numerically simulated waves were compared to waves of a single experimental run.

The geometry of the NPS tow tank and its wave maker are unique. Accordingly, the waves generated by a given wedge command are as unique as the facility. Commanding the wedge to oscillate at a certain amplitude and frequency will not necessarily produce waves with

identical oscillatory behavior. A transfer function was developed to relate wedge amplitude to resultant wave height. Tested frequencies ranged from 0.75 Hz to 1.5 Hz. Five amplitudes ranging from 0.635 centimeters (0.25 inches) to 5.08 centimeters (2.0 inches) were tested at each frequency. Experimental and numerical transfer functions were compared to validate the simulations.

Finally, three-dimensional forces and moments observed by a submerged body were tested. The body is a simple rectangular prism with a square cross section. The width of the body, W_B, is 10.16 centimeters (4.0 inches) and the length, L_B, is 1.016 meters (40.0 inches), corresponding to an aspect ratio of 10. The body was 3D printed by a Fortus 400mc rapid prototyping machine and is composed of polycarbonate. It was assembled as three 25.4 centimeter (10.0 inch) segments, one 15.2 centimeter (6.0 inch) segment, and two 5.08 centimeter (2.0 inch) end caps. Due to size limitations of the 3D printer, the body had to be printed in sections rather than a single piece. The assembled body is shown in Figure 3.5.

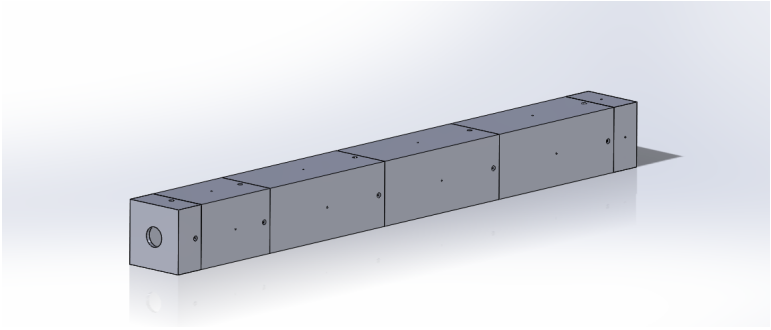

Figure 3.5. CAD model of 3D printed body inserted into experimental wave tank.

The aft end has a 3.175 centimeter (1.25) inch diameter hole in its center to allow a sting through the body. The sting keeps the segments rigid and straight as the waves pass over. The support arm extends out the back of the body and up to connect directly to the load cell.

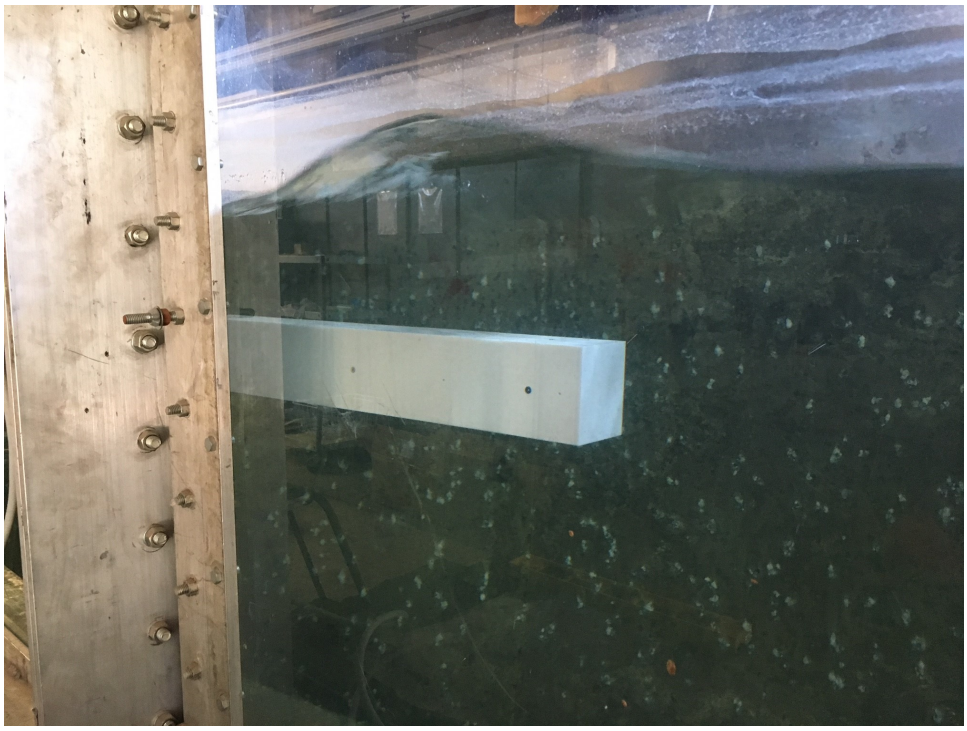

Figure 3.6. Square cross section body submerged in tow tank at a centerline depth of 20.32 centimeters (8.0 inches).

The center of the body was placed 2.74 meters (9.0 feet) from the wedge. Two series of tests were done, one at a center line depth of 20.32 centimeters (8.0 inches), and another at a center line depth of 10.16 centimeters (4.0 inches). These depths correspond to a nondimensionalized depth of $d/W_B = 2$ and $d/W_B = 1$. Nondimensional wavelengths (λ/L_B) varying from 0.5 to 2 were generated with a wave amplitude of 2.54 centimeters (1.0 inch), and resultant forces and moments were observed by the load cell. Figure 3.6 shows the submerged body in the test setup with waves passing over it.

THIS PAGE INTENTIONALLY LEFT BLANK

CHAPTER 4:
Numerical Setup

The numerical simulation of the tow tank's wave environment was done in ANSYS CFX version 17.2. The tank and wedge geometries were duplicated in SOLIDWORKS 2015 as closely as possible. Figure 4.1 is a side view of the fluid domain used in ANSYS CFX.

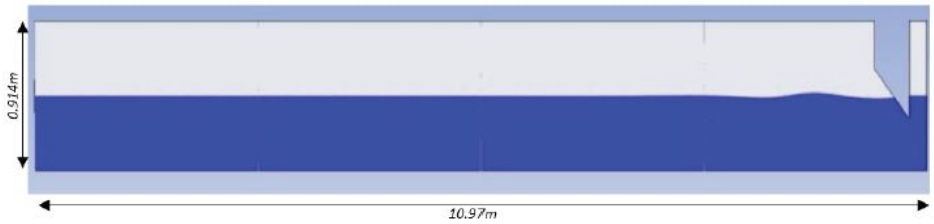

Figure 4.1. Side profile of numerical wave tank and wedge within ANSYS CFX.

Figure 3.1 details the geometry of the numerical wedge. Its face is 35 degrees from the vertical and is 0.61 meters (2.0 feet) tall. In both two-dimensional and three-dimensional simulations, the wedge spans the width of the numerical tank. A gap of 0.203 meters (8.0 inches) is behind the wedge, which is identical to the physical wedge setup.

4.1 Tank Physics

The fluid domain was modeled as fresh water at 25°C and air at 25°C. Both were at a reference pressure of 1 atmosphere. The calm water height was 0.914 meters (3.0 feet). Gravity was modeled as 9.81 m/s^2 (32.2 ft/s^2). A $k-\epsilon$ turbulence model was used to capture the effects of turbulence.

4.1.1 Wedge Motion

The wedge was defined as a boundary to the meshed fluid domain. The mesh that composed the wedge deformed according to the commanded wedge displacement. Wedge displacement was defined according to Equation (4.1).

$$z = \left(1 - e^{(-3t^2)}\right) a_w \sin(2\pi f t + \phi) \tag{4.1}$$

where a_w is the wedge amplitude, f is the oscillation frequency, ϕ is the phase (kept to zero for all simulations in this study), and z is vertical wedge displacement. The exponential term in front of a_w models the buildup of the wedge displacement to its full amplitude. The physical wedge also has a start-up behavior that is reasonably captured with this equation.

4.1.2 Boundary Conditions

The initial parametric study was kept as a two-dimensional fluid domain in order to run full simulations in relatively short computational time. For these two-dimensional simulations, the tank was 0.02 meters thick, and the side walls were modeled as symmetries. Symmetries in ANSYS CFX are free-slip boundaries, which have zero shear stress, effectively infinitizing the domain in the direction normal to the boundary. The side walls were changed to no-slip smooth walls in the three-dimensional case. The tank back, tank bottom, tank front, and wedge were all modeled as no-slip smooth walls. The top of the tank was modeled as an opening, which allowed only air to pass in and out of the domain according to the local pressure at the boundary.

4.2 Parametric Study of Modeling Conditions

A number of user-defined parameters may be manipulated in ANSYS CFX. These parameters affect model convergence, computational time, and model accuracy. They must be adjusted according to the given problem one wishes to study. The parameters that were adjusted in this study were mesh shape, mesh size, and time step. Each were altered while other variables were kept constant to determine the effect each parameter had on model performance. For the following parametric study, all simulations used a wedge oscillating at 2.54 centimeters (1.0 inch) in amplitude and 1 Hz in frequency.

4.2.1 Mesh Size

Mesh size influences the results of a numerical simulation. Typically higher resolution meshes yield more accurate results. Many simulations will not reach convergence if the mesh is not fine enough. It is for this reason that the area immediately above and below

the free surface (the area with the most fluid movement) is more refined than the rest of the domain. Higher mesh resolution, however, drastically increases computational time. A parametric study was done to find the most accurate practical mesh face size in the two-dimensional case. Face size varied from 2.5 millimeters (0.984 inches) to 10 millimeters (0.394 inches), corresponding to 624.5 elements per wavelength and 156.1 elements per wavelength. All other parameters were held constant.

4.2.2 Mesh Shape

A meshing algorithm inherent to the ANSYS CFX software suite is responsible for constructing a mesh that fits the size and shape of the fluid domain. The user may define the shape of the two-dimensional or three-dimensional elements that compose the domain. The most common volume element shapes are tetrahedral and hexahedral, shown in Figure 4.2.

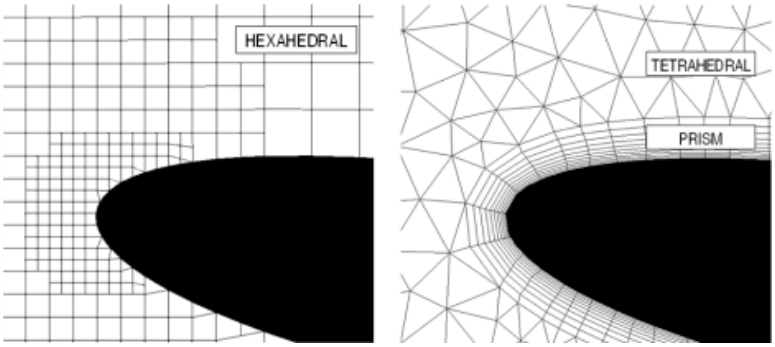

Figure 4.2. The same fluid domain meshed with hexahedrons (left) and tetrahedrons (right). Source [16].

Tetrahedral mesh has triangular shaped faces and is effective for meshing curves, sharp angles, and complex geometries. However, tetrahedral meshes tend to require many more elements to render a domain. Hexahedral mesh has rectangular faces and is brick shaped. Meshing with hexahedrons is much more computationally efficient but requires much more user intervention to mesh around complex geometries.

In the numerical wave tank, the mesh 0.229 meters (9.0 inches) above and below the free surface was much more refined to more accurately capture fluid behavior, as shown in Figure 4.3. The face size of these refined elements were varied from 1.25 millimeters

(0.044 inches) to 10 millimeters (0.394 inches) for both mesh shapes, corresponding to nondimensionalized resolution quantities of 1249.0 elements per wavelength and 156.1 elements per wavelength, respectively. A parametric study was done to determine the optimal meshing technique for the given scenario. Computational effort (total number of elements required to mesh the domain) and accuracy of wave height were considered to determine the ideal mesh shape for the rest of the study. Figure 4.3 shows the meshed fluid domain with a highly refined band at the free surface.

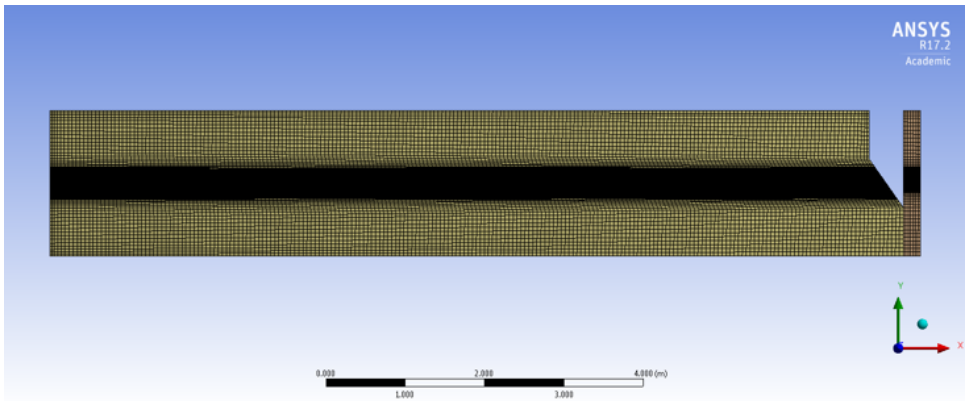

Figure 4.3. Meshed tank fluid domain.

4.2.3 Time Step

Time step size in transient CFD simulations plays a role in simulation accuracy. A smaller time step generally leads to better convergence at a cost of more computing time required. A study was done to determine the effect that different time steps had on wave amplitude. Time step size was varied from 0.0025 seconds to 0.01 seconds, corresponding to nondimensionalized time resolutions of 400 time steps per wave period and 100 time steps per wave period, respectively. Performance factors considered were simulation computational time and accuracy of wave height.

4.2.4 3D versus 2D Simulations

Finally, a study was done to compare a three-dimensional numerical tank model to a two-dimensional one. Computing time for the three-dimensional case was on the order of ten times longer, but more accurately reflects the experimental setup. The width of the tank

was extended to 0.9144 meters (3.0 feet) and the side walls were treated as smooth no-slip boundaries rather than free-slip symmetries. The same mesh refinements used in the two-dimensional size study were observed in the three-dimensional simulations. Time step and mesh shape were held constant. Simulated three-dimensional wave amplitudes were compared to those generated by the two-dimensional simulations and the experimental case.

4.3 Obtaining a Wedge-Wave Transfer Function

A transfer function relating wedge amplitude to wave amplitude was developed to determine the required wedge command to produce the desired waves for a given oscillatory frequency. A transfer function was developed for the numerical domain by relating Stokes wave height to twice the commanded wedge amplitude. The tested wedge amplitudes ranged from 6.35 millimeters (0.25 inches) to 50.8 millimeters (2.0 inches) and wedge frequencies ranged from 0.75 Hz to 1.25 Hz.

4.4 Transient Forces on a Submerged Body

After developing transfer functions for both domains, force and moment analysis for single-component waves was done on a near surface submerged body. The body used in CFD analysis was of the same geometry as the body used in the experimental setup. It was placed in the same position in the tank (2.74 meters from the wedge and 20.32 centimeters in depth).

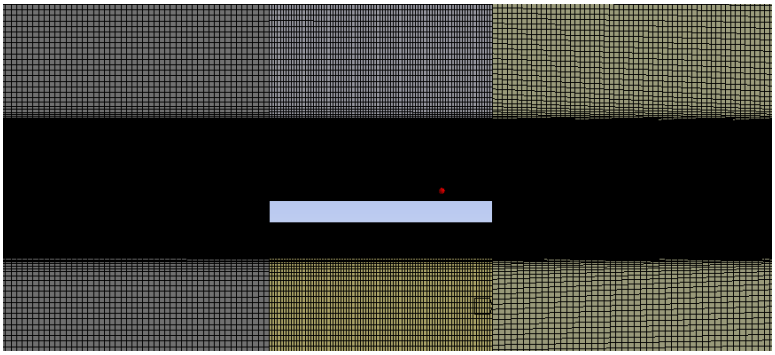

Figure 4.4. Cross section of meshed fluid domain with body inserted.

In the ANSYS CFX solver, the submerged body was treated as a fixed rigid body. The body's

center of gravity and center of buoyancy were placed at the centroid. Time histories of vertical force and moment about the centroid were observed for 16 seconds. Nondimensional wavelengths (λ/L_B) of 0.625, 0.75, 0.875, 1.0, 1.125, 1.25, 1.375, 1.5, 1.6, 1.7, 1.8, and 2.0 were generated at a wave amplitude of 2.54 centimeters.

CHAPTER 5:
Results and Discussion

5.1 Numerical Wave Tank Parametric Study

5.1.1 Determination of Mesh Size

Mesh face size was varied from 2.5 millimeters to 10 millimeters and resultant wave heights at various tank locations were compared to the physical case. Commanded wedge amplitude and frequency were 2.54 centimeters and 1 Hz, respectively. Amplitude readings by the probes located at 2.74 meters (9.0 feet), 5.49 meters (18.0 feet) and 8.23 meters (27.0 feet) are shown in Figure 5.1.

It is clear from Figure 5.1 that the amplitudes of the waves in the numerical simulations are slightly smaller in magnitude than those generated experimentally. However, the general shape of both experimental and numerical waves are very similar. The wave frequencies are all identical. Additionally, numerical and experimental wave packets show an initial slight spike of wave height followed by a roughly constant-amplitude series of waves.

A sinusoidal curve fit function was applied to the time history wave elevation data in a least-squares sense to determine first-order amplitude. The wave height was then estimated by applying the first-order amplitude to the Stokes wave height formula along with the corresponding wave number. Wave height from each simulation at each probe was compared to experimental wave height via a wave height ratio (identical waves would have a ratio of one). Results are shown in Figure 5.2.

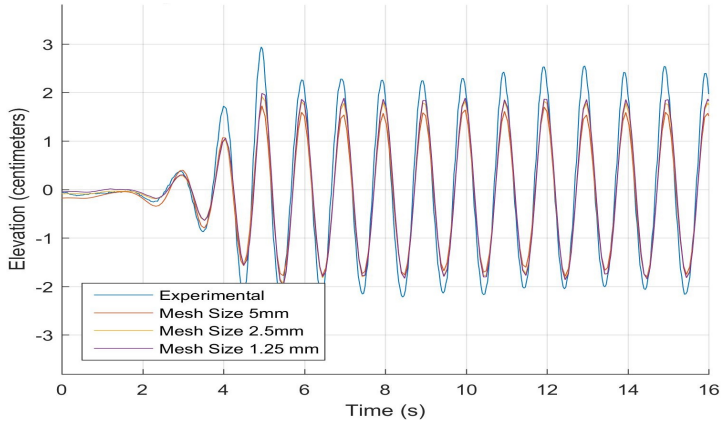

(a) x/L=0.25 (9 feet).

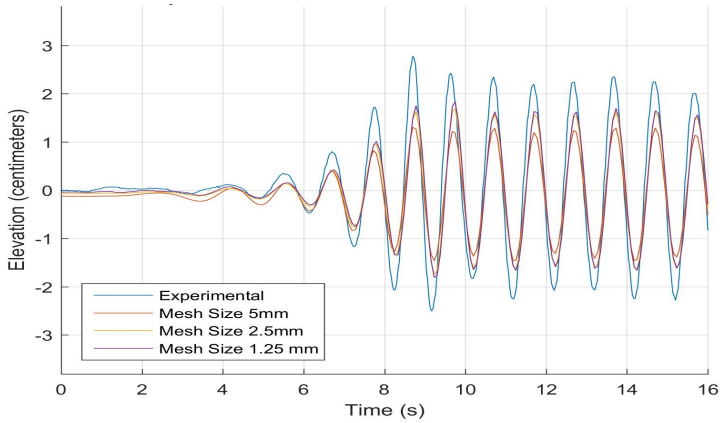

(b) x/L=0.5 (18 feet).

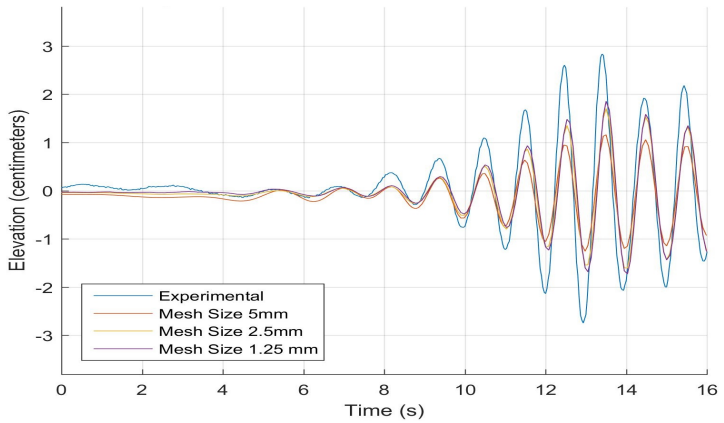

(c) x/L=0.75 (27 feet).

Figure 5.1. Wave amplitude readings from both the physical and numerical domain at different locations in the tank.

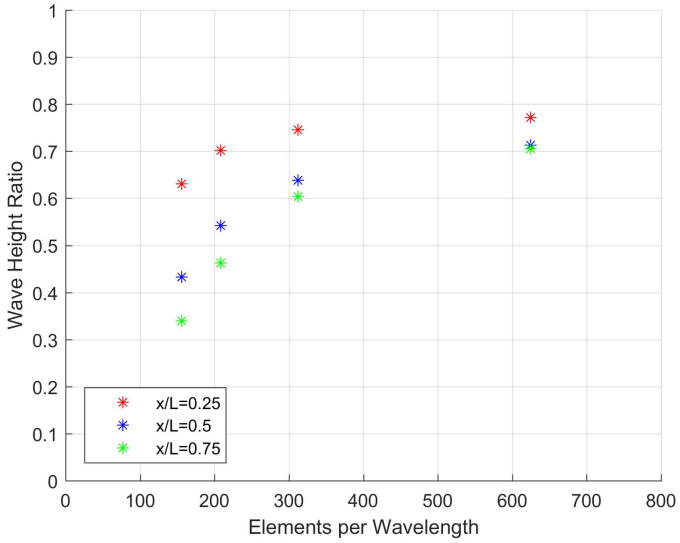

Figure 5.2. Height ratio comparing simulation wave height to experimental wave height for various mesh sizes.

Figure 5.2 shows that decreasing the mesh size improves accuracy of the results. However, even the most accurate run achieved only 77.3% of experimentally measured wave height at the x/L=0.25 probe. Additionally, less artificial wave dissipation down the length of the tank occurs as mesh size is decreased. The 2.5 millimeter (624.5 elements per wavelength) simulation achieved 10.36% dissipation from the first probe to the third probe, as opposed to 45.2% dissipation in the 10 millimeter (156.1 elements per wavelength) case. Computational time increases exponentially for each reduction in mesh size, making simulations refined much more than 2.5 millimeters impractical. A mesh face size of 2.5 millimeters was used for the rest of the study.

5.1.2 Determination of Mesh Shape

The size study discussed in the previous section used tetrahedral mesh. A similar size study was done for hexahedral mesh, and the results were compared. Figure 5.3 shows the height ratio results for various mesh sizes of both mesh shapes.

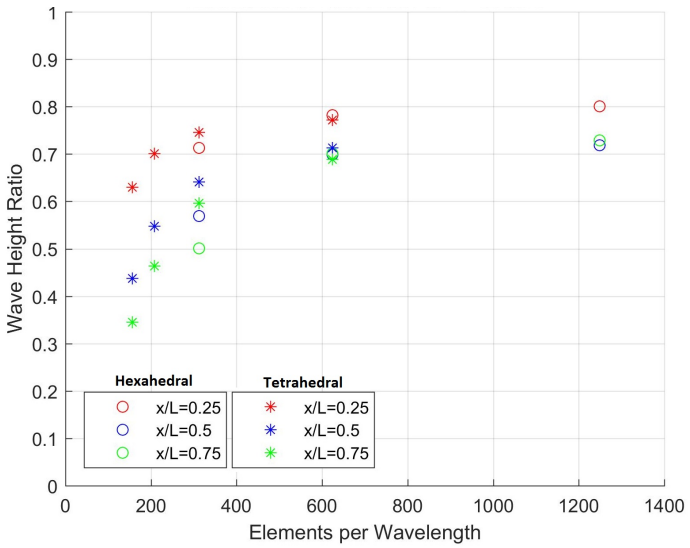

Figure 5.3. Height ratio comparing simulation wave height to experimental wave height for various mesh sizes of tetrahedral and hexahedral mesh.

The wave height ratio of simulated waves for identical mesh face sizes is virtually identical between the tetrahedral and hexahedral case. At a face size of 1.25 millimeters, the hexahedral mesh was able to achieve a wave height ratio of 80.1% at the x/L=0.25 probe. The same case also achieved 10.2% dissipation from the first to the third probe. Hexahedral meshing requires more user intervention to ensure neatly structured mesh, but can achieve a high resolution grid using far fewer elements. The result is that simulation run times for hexahedral cases were much shorter than their tetrahedral counterparts. Rendering a fluid domain with a smaller mesh face size was much more computationally practical when using hexahedrons. Table 5.1 shows the number of elements rendered in the two-dimensional case for various face sizes of the two different meshing techniques. The ratio of tetrahedrons to hexahedrons rendered for a given mesh face size is given in the last row.

Number of Elements		Mesh Face Size (mm)				
		1.13	2.50	5.00	7.50	10.00
Mesh Type	Tetrahedral		35,700,000	4,800,000	1,540,000	695,000
	Hexahedral	71,900	41,400	25,100	18,900	16,300
	T/H Ratio		862.32	191.24	81.48	42.64

Table 5.1. Number of elements rendered for various face sizes of both meshing techniques.

Simulations done using hexahedral elements were completed much faster than tetrahedral simulations. Hexahedral mesh with a free surface face size of 2.5 millimeters (624.5 elements per wavelength) was used going forward.

5.1.3 Determination of Time Step

Simulations were run at various time steps in two dimensions with a constant mesh face size of 2.5 millimeters and hexahedral mesh. The wave height ratios for the various temporal resolutions are outlined in Figure 5.4.

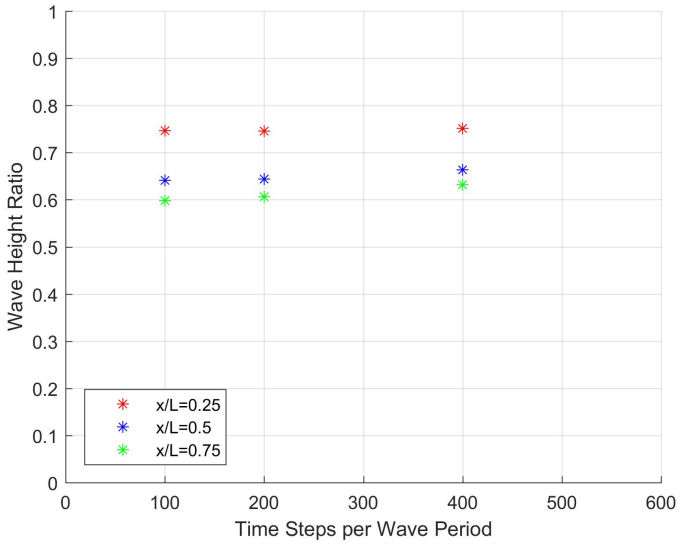

Figure 5.4. Wave height ratio for various time steps.

The data shows that decreasing the time step to less than 100 time steps per wave period

(0.01 seconds) contributes negligible simulation accuracy while increasing computational time. A time step of 0.01 seconds was maintained for the rest of the simulations.

5.1.4 Three-Dimensional versus Two-Dimensional Simulation

Simulations were expanded to the three-dimensional case to better reflect physical tank conditions. The three-dimensional case was fifty elements deep in the z direction, meaning that each rendering consisted of fifty times more elements than the two-dimensional case. Computational times were much longer. The three-dimensional fluid domain was rendered with mesh face sizes of 2.5 millimeters (624.5 elements per wavelength), 3.75 millimeters (416.3 elements per wavelengths), and 5.0 millimeters (312.3 elements per wavelength). Wave height ratios were determined at each probe and compared to the two-dimensional case.

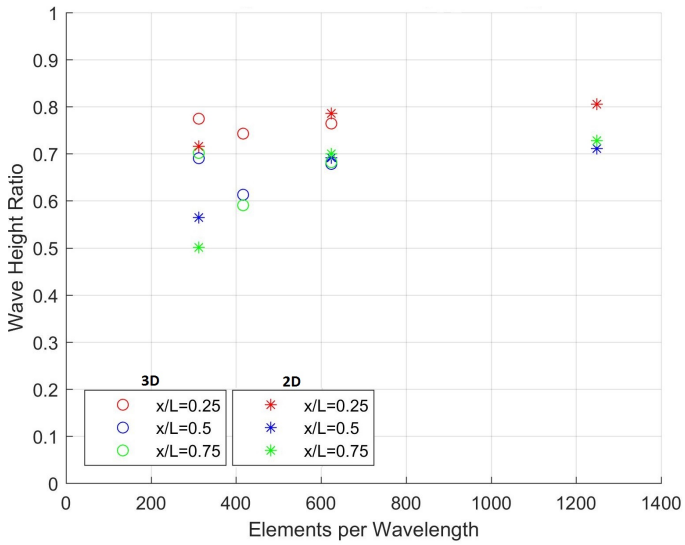

Figure 5.5. Wave height ratio for various mesh face sizes in both the 3D and 2D case.

For the 2.5 millimeter case in three dimensions, the height ratio at each probe is only between 1.0% and 1.9% less than the two-dimensional height ratio. Simulations for the rest of the study were kept in three dimensions and a mesh face size of 2.5 millimeters (624.5 elements per wavelength) was used.

5.2 Wedge-Wave Transfer Function

Despite mesh refinement, simulations produced waves slightly shorter in height than the experimental case. In order to ensure that the waves passing over a submerged body in future experiments and simulations were as similar as possible, transfer functions had to be used to relate wedge amplitude to wave height for both the experimental and numerical case. The transfer function is defined as $\Psi = \frac{H}{2a_w}$. In Figure 5.6, Ψ is shown for both the physical and numerical tank as a function of wedge frequency.

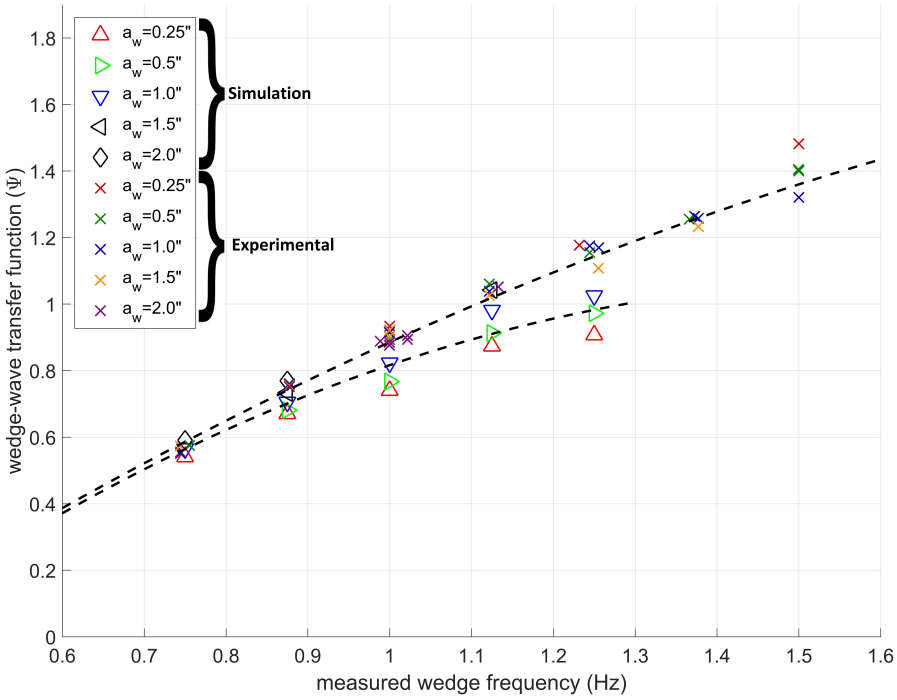

Figure 5.6. Transfer function relating wave height to wedge amplitude.

A second-order polynomial curve fit was used to fit both data sets. These two polynomials were then used to determine the required wedge amplitudes for the tow tank and the simulations so that each produced a wave amplitude of 2.54 centimeters (1.0 inch). The transfer functions ensure that wave height is consistent between corresponding experiments and simulations. Lower frequency simulated waves behave much more like their experimentally generated counterparts. Simulated waves of frequency 0.75 Hz to 0.875 Hz show

heights of 88.6% to 99.1% of the same experimental waves. Additionally, there is much less height variance among different wedge amplitudes at these low frequencies. High frequency simulations (1.0 Hz to 1.25 Hz) show much more variance among different wedge amplitudes and are 78.2% to 85.1% accurate.

5.3 Force and Moment Analysis

Time histories of body forces and moments were recorded for a wave amplitude of 2.54 centimeters (1.0 inch) and a body center line depth of 20.32 centimeters (8.0 inches). Nondimensional wavelengths varied from 0.625 to 2.0 in the numerical case. A large number of data points were collected in the experimental case to develop well defined force and moment curves. Example time histories of force and moment from the $\lambda/L_B = 1.375$ simulation are shown in Figure 5.7.

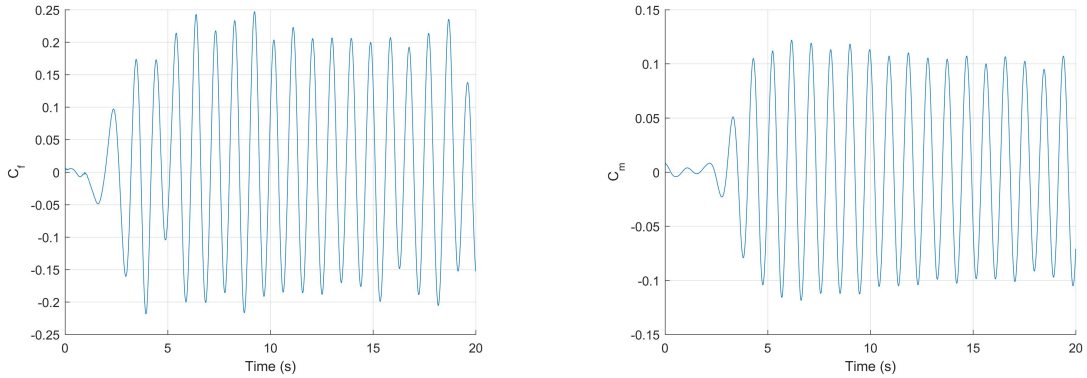

(a) Nondimensionalized Force. (b) Nondimensionalized Moment.

Figure 5.7. Simulation force and moment time history for $\lambda/L_B = 1.375$ case.

For each experimental run and simulation, a sine wave with frequency equal to the wedge oscillation was fit to the steady portion of the force and moment time history data in a least-squares sense to determine the oscillation amplitude of each. In Figure 5.7, the steady portion of the signals was considered to begin at 10 seconds. The steady state frequency of the force and moment oscillations was exactly equal to the wedge (and wave) frequency. Figure 5.8 shows nondimensionalized force and moment coefficients for both the experiment

and simulation as a function of nondimensional wavelength. Force and moment coefficients are defined by Equation (5.1) and Equation (5.2).

$$C_f = \frac{F}{\rho g L_B W_B a} \tag{5.1}$$

$$C_m = \frac{M}{\rho g L_B^2 W_B a} \tag{5.2}$$

The experimental force results show that there are two distinct curves that exist over this span of wavelengths with a local maximum on the lower wavelength curve and a global maximum on the higher wavelength curve. A local minimum exists at $\lambda/L_B = 0.85$, where the force felt by the body drops to nearly zero. At $\lambda/L_B = 0.8125$ and $\lambda/L_B = 0.9375$ the experimental data varies significantly from the trend. These points were tested four times each, producing similar results. A possible explanation is that this wave frequency matches the resonant frequency of the sting holding the body, causing a sudden jump in applied force at a particular frequency. The experimental moment results show a similar trend of two local maxima, with the higher wavelength maximum being greater in magnitude. There is a minimum in the moment data at $\lambda/L_B = 0.6875$ where the moment felt by the body drops to nearly zero.

The simulation force data has a lower "hump" similar to the experimental data. This hump and its corresponding local maximum, however, occur at a slightly larger nondimensional wavelength. Simulation force amplitudes of higher wavelengths approach a maximum force in a similar manner to the experimental force amplitudes. However, these numerically predicted forces at nondimensionalized wavelengths of 1.5 and greater are significantly larger than the forces recorded experimentally. In the nondimensional wavelength range of 1.125 to 1.375, simulation force amplitudes closely predict physical loads. The simulation moment data much more closely fits the experimental data points, especially at lower frequencies. The moment data reaches a global maximum at $\lambda/L_B = 1.6$. The predicted nondimensionalized moment at this wavelength is about 40% larger than the experimentally observed moment, which occurs at a smaller wavelength.

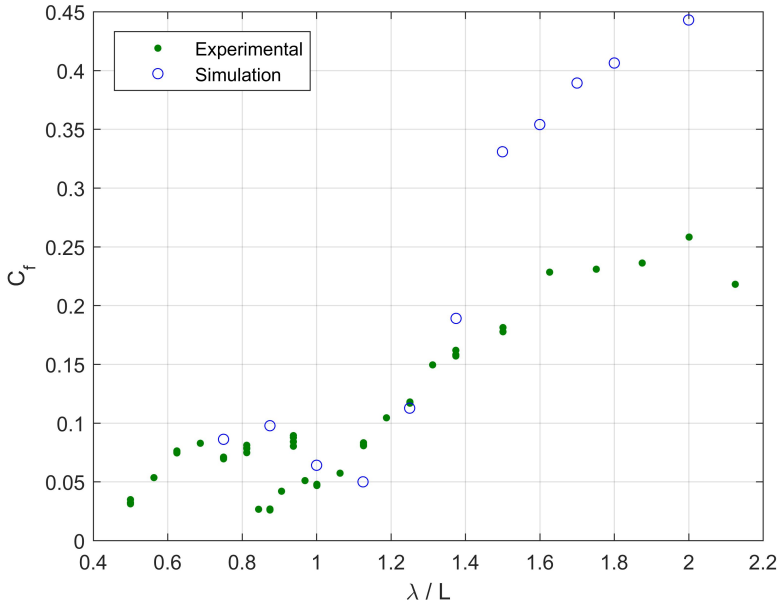

(a) Force amplitudes for a variety of wavelengths.

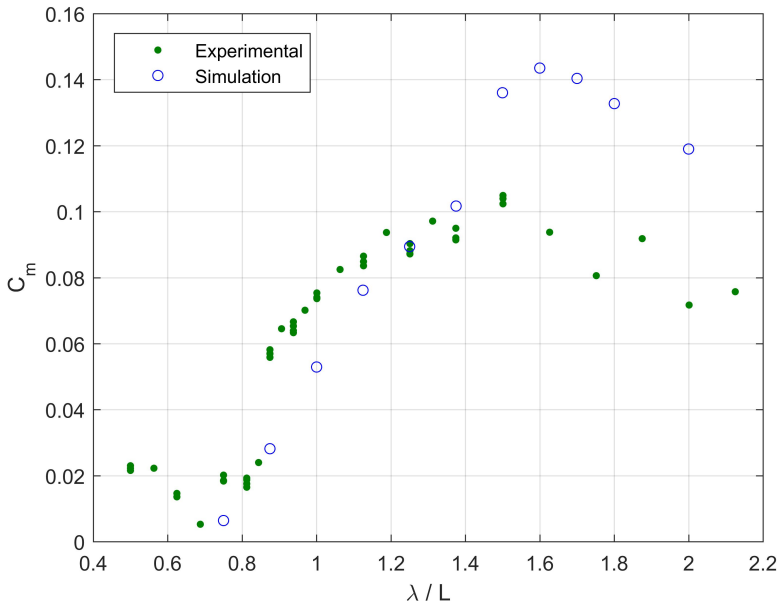

(b) Moment amplitudes for a variety of wavelengths.

Figure 5.8. Experimentally measured and numerically predicted amplitudes of the wave-induced oscillating vertical force and pitching moment on a submerged body near the surface as a function of nondimensional wavelength.

An identical study was conducted with the body at a center line depth of 10.16 centimeters (4.0 inches). The simulation conditions were identical to the 20.32 centimeters (8.0 inches) depth case, yet the force and moment time histories were too chaotic and random in nature to have the amplitude of a least-squares fit sine wave be meaningful in any manner. As a result, the simulation force and moment amplitude data points did not form a coherent trend and were significantly different from the experimentally generated curves, which did show strong periodic loading. The simulation results for the $\lambda/L_B = 0.625$ case is shown in Figure 5.9 as an example.

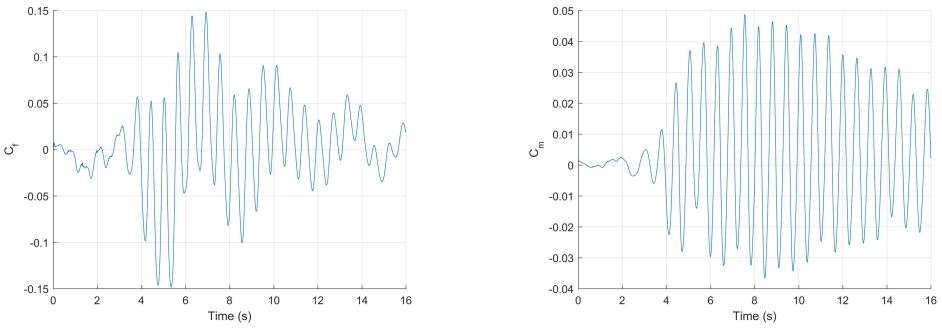

(a) Force time history ($\lambda/L_B = 1.375$). (b) Moment time history ($\lambda/L_B = 1.375$).

Figure 5.9. Simulation force and moment time history for $\lambda/L_B = 0.625$ and $d/W_B = 1$ case.

The irregularity of the simulation force and moment data for a very shallow body is likely due to the relatively high velocity fluid striking the blunt front of the body. This effect requires much higher resolution mesh in the vicinity of the body in order to ensure more accurate interaction with the fluid and rigid surface. Additionally, a very shallow body induces irregular wave effects, similar to waves breaking on a beach. This "breaking" phenomenon is much more random and irregular than smooth, non-breaking waves in terms of observed body force. The current mesh refinement may not be able to accurately resolve the breaking of waves passing over the model. This leads to non-periodic loads in the simulation. In the experiment, the shallowness of the body does disturb the waves, but they still maintain coherent form and produce periodic loading. Higher resolution mesh around the body will be necessary for more accurate results in very shallow cases. Figure 5.10 shows how a very shallow body disturbs the waves passing over it.

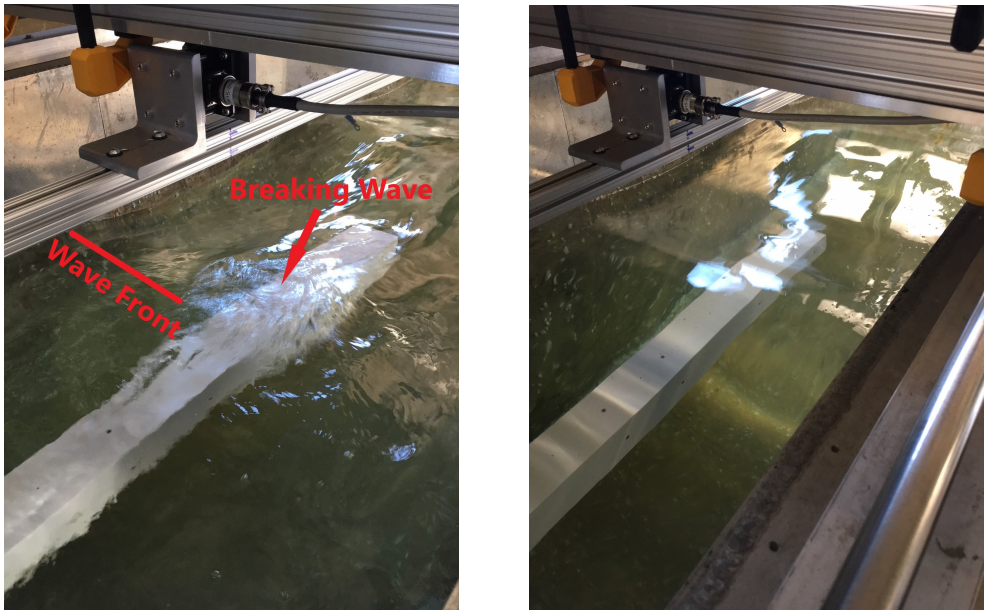

Figure 5.10. Waves becoming incoherent as they pass over a very shallow body ($d/W_B = 1$), shown left, compared to waves passing coherently over a deeper body ($d/W_B = 2$), shown right.

CHAPTER 6:
Conclusions and Future Work

The strong dependence that grid size, grid shape, and time step have on numeric accuracy and computational time necessitated that a parametric study be conducted to optimize them. It was determined that a three-dimensional simulation of waves in the tank was feasible when 2.5 millimeter hexahedral mesh was rendered at the free surface and simulations were conducted with a time step of 0.01 seconds. Accuracy of generated wave heights varied with wave frequency. At lower frequencies (0.75 Hz to 0.875 Hz), simulated wave heights were very accurate, with simulated Stokes heights ranging from 88.6% to 99.1% of experimental heights and negligible dissipation. At higher frequencies, it was found that dissipation increases and simulated waves are 78.2% to 85.1% as high as experimental waves.

At a body depth of twice the cross sectional width (20.32 centimeters) and wave amplitude of 2.54 centimeters, the general behavior of the amplitude of the predicted oscillating force resembled that of the corresponding experimental cases. The trend was slightly shifted, however, with a force minimum and local maximum occurring at a slightly higher wavelength. The moment data much more closely resembled the experimental results at low to middle range nondimensionalized wavelengths. A broader testing matrix is needed in the future to better understand how the simulation body force and moment relate to the experimental results. Different depths, wave heights, and body geometries will need to be considered.

CFD has been proven as a valuable method of augmenting studies conducted in the NPS tow tank. Future tests involving wave generation can be conducted numerically before physical models are used in the tank. Effectively using a numerical model to represent physical phenomenon requires comprehensive understanding of the behavior of the model for the desired application. A great advantage of CFD is also its great challenge—physical phenomena are not automatically defined like they are in the real world. The proper physical models and constants must be applied, tested, and evaluated before any merit can be given to their results. This study accomplished that for the specific domain that is the NPS tow tank with wedge-driven wave generation.

The goal of this study was to validate CFD as a useful tool in the endeavor of studying, quantifying, and predicting wave behavior of a wedge-type wave maker and resultant loads on near-surface submerged bodies. While many more simulations must be refined and conducted to expand the robustness of CFD for this specific application, great understanding has been developed in regard to simulated waves.

6.1 Future Work

Additional mesh refinement is necessary to improve simulation accuracy at higher oscillation frequencies. Under current model conditions, simulations conducted at wedge frequencies of 1.0 Hz and higher produce waves that are 14.9% to 21.8% shorter than physical waves generated under the same wedge conditions. Additionally, mesh resolution should be increased around the body to see if wave irregularities may be more accurately captured. A higher resolution grid may also solve the inaccuracies of the predicted force and moment amplitude curves.

This study only examined forces and moments experienced by a submerged body at one depth and one wave height. The logical next step is to conduct the same force and moment study at a wide breadth of wave heights and body depths. Next, forward velocity should be applied to the body to examine how this impacts the transient forces and moments. After extensive exploration in a physical and numerical test facility, predictive force and moment algorithms may be developed for the given geometry. With body depth, body velocity, wave height, and wavelength, one could predict the steady state loads that the submersible will perceive.

A simple square cross section prism was used as the submerged body in this study. Obviously, a submersible with any intention of being hydrodynamically efficient would avoid this shape, but rendering hexahedral mesh around square corners is much simpler than rendering around curves. The square body was used as a proof of concept to see if force and moment simulations could practically be compared to results. The next step to apply the findings of this study will be to swap the square body for a rounded, axisymmetric one. Eventually, a CAD model of an actual UUV or submarine may be used. This will require much more user intervention and sophistication in the meshing process, but once a mesh is rendered, simulations will be identical to the square body case. Overall, the results of this

study are promising yet show room for fine tuning to better develop an accurate numerical representation of a complicated physical phenomenon.

THIS PAGE INTENTIONALLY LEFT BLANK

List of References

[1] R. M. Tran, "Evaluation of composite-hull ships operating in arctic ice," Master's thesis, Dept. of Mechanical and Aerospace Engineering, NPS, Monterey, CA, USA, 2016.

[2] W. E. Landay, M. A. LeFever, R. A. Spicer, R. M. Levitre, S. J. Toamszeski, J. A. Walsh, and R. M. Smith, "The Navy unmanned undersea vehicle (UUV) master plan," 2006.

[3] J. L. V. Belle. (2014). Bad thinking: Photons versus the matter wave. Reading Feynman. [Online]. Available: https://readingpenrose.files.wordpress.com/2014/04/dispersion.jpg

[4] L. Schwartz and J. Fenton, "Strongly nonlinear waves," *Annual Review of Fluid Mechanics*, vol. 14, pp. 39–60, 1982.

[5] G. Stokes, "On the theory of oscillatory waves," *Transactions of the Cambridge Philosophical Society*, vol. 8, pp. 197–229, 1847.

[6] W. Finnegan and J. Goggins, "Numerical simulation of linear water waves and wave-structure interaction," *Ocean Engineering*, vol. 43, pp. 23–31, 2011.

[7] S. Yim, D. Yuk, A. Panizzo, M. D. Risio, and P. Liu, "Numerical simulations of wave generation by a vertical plunger using RANS and SPH models," *Journal of Waterway, Port, Coastal, and Ocean Engineering*, vol. 134, pp. 143–159, 2008.

[8] J. Gadelho, A. Lavrov, C. G. Soares, R. Urbina, M.P. Cameron, and K.P. Thiagarajan, "CFD modeling of the waves generated by a wedge-shaped wave maker," in *Maritime Technology and Engineering*, C. Guedes Soares and T. A. Santos, Eds. London, UK: Taylor & Francis Group, 2014. pp. 993-1000.

[9] A. Alvarez, V. Bertam, and L. Gualdesi, "Hull hydrodynamic optimization of autonomous underwater vehicles operating at snorkeling depth," *Ocean Engineering*, vol. 36, pp. 105–112, 2008.

[10] W. E. Cummins, "Forces and moments acting on a submarine moving under waves - comparison of theory with experiment," Navy Department, Tech. Rep., 1954, report 780.

[11] G. Khalil, "Experimental investigation of wave forces on submerged horizontal cylinders," *Indian Journal of Engineering & Materials Science*, vol. 8, pp. 59–65, 2001.

[12] ANSYS, *ANSYS CFX-Solver Theory Guide*, 11th ed., ANSYS, Inc., Canonsburg, PA, USA, 2011. Available: http://product.caenet.cn/Uploadfiles/128724372509866250200811290900509 86.pdf

[13] N. Hall. (2015). Navier-Stokes equations. National Aeronautics and Space Administration. [Online]. Available: https://www.grc.nasa.gov/www/k-12/airplane/nseqs.html

[14] S. V. Patankar, *Numerical Heat Transfer and Fluid Flow*. Washington, USA: Hemisphere Pub. Corp., 1980. Available: http://www.ebook.de/de/product/7285606/suhas_v_patankar_numerical_heat_transfer_and_fluid_flow.html

[15] M. W. Dingemans, *Water Wave Propagation Over Uneven Bottoms (in 2 Parts)*. Singapore, World Scientific Pub. Co. Inc., 1997.

[16] J. Chilvers. (2014). The Finite Volume Method: An Introduction. [Online]. Available: https://tameaero.wordpress.com/2014/10/24/the-finite-volume-method-an-introduction/

Initial Distribution List

1. Defense Technical Information Center
   Ft. Belvoir, Virginia

2. Dudley Knox Library
   Naval Postgraduate School
   Monterey, California